

Supplementary Materials for
**Constraining the entire Earth system projections for more reliable climate
change adaptation planning**

Chao Li *et al.*

Corresponding author: Chao Li, cli@geo.ecnu.edu.cn

Sci. Adv. **11**, eadr5346 (2025)
DOI: 10.1126/sciadv.adr5346

This PDF file includes:

Figs. S1 to S18
Tables S1 to S3

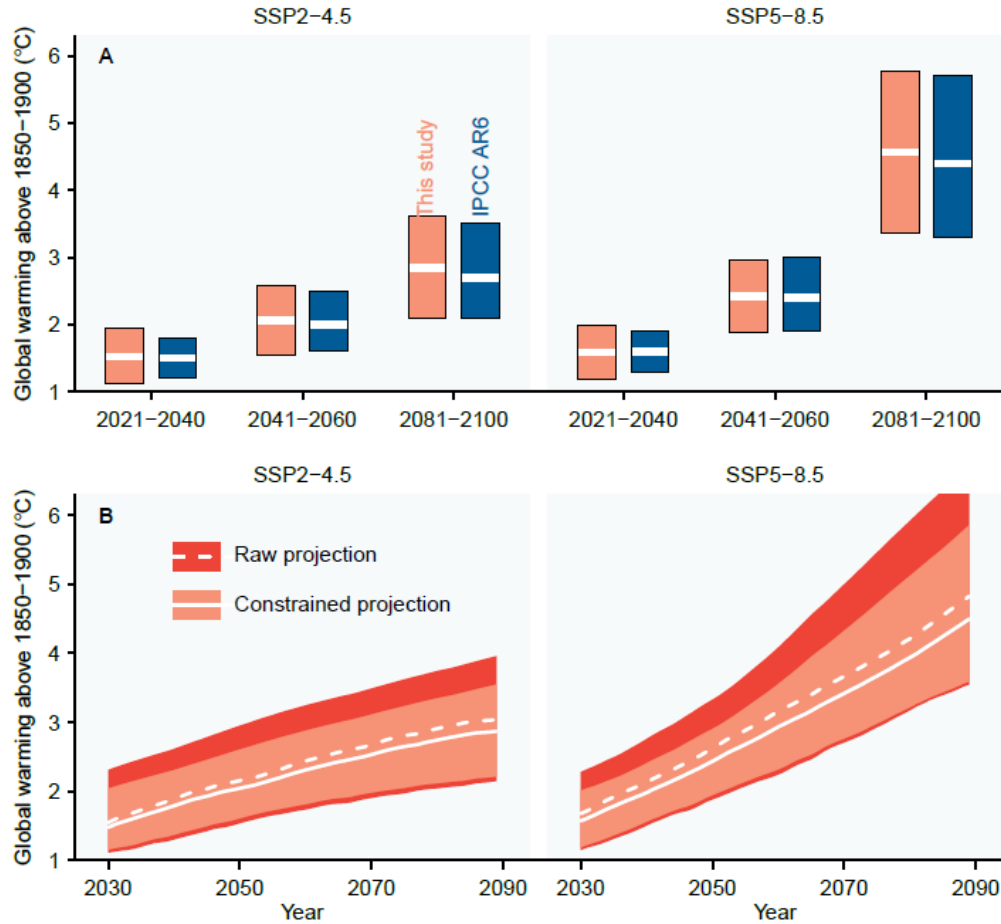


Fig. S1. Comparison of constrained global warming projections. (A) The global warming projections for three selected 20-year periods relative to 1850-1900 derived by the emergent constraint using the observed warming during 1971-2020 in HadCRUT5 as an observational constraint (light orange bars) and the assessment results in IPCC AR6 (blue bars). The colored bars and white horizontal lines mark the very likely (5-95%) ranges and means of the warming projections, respectively. In addition to different methods, the two results are also based on different Earth system models. (B) Time series of global warming projections for 20-year moving windows from 2021-2040 to 2081-2100 relative to 1850-1900 derived from raw, unconstrained projections (orange) and projections constrained by emergent constraint using the observed warming during 1971-2020 in HadCRUT5 as an observational constraint (light orange). The shading and white curves mark the 5-95% ranges and means of the warming projections, respectively. Left and right panels show the results for SSP2-4.5 and SSP5-8.5 emissions scenarios, respectively.

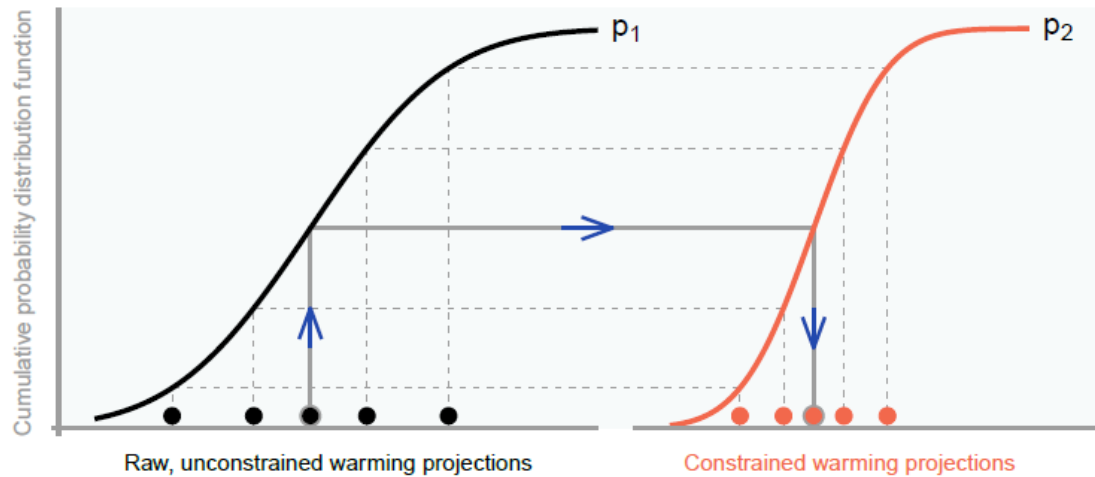


Fig. S2. A schematic illustration of the quantile mapping process. The quantile mapping method transforms the quantiles of the prior projection warming distribution p_1 , i.e., the raw, unconstrained global warming projections from individual climate models, to the corresponding quantiles of the posterior warming distribution p_2 , producing constrained warming projections for individual climate models. Note the one-to-one correspondence between unconstrained and constrained projections for individual models.

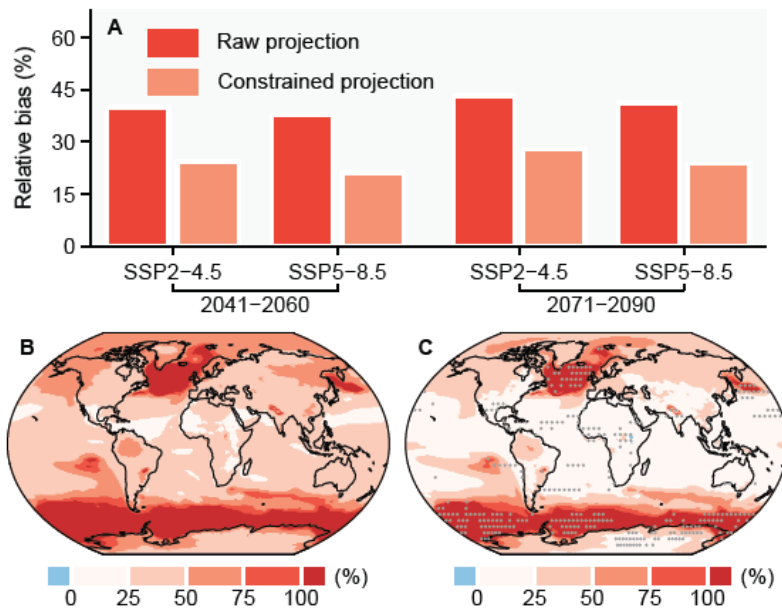


Fig. S3. Model-based evaluation of the constrained level-of-global warming approach with respect to relative warming bias. As in Fig. 2 in the main text, but for evaluation with respect to relative biases in the estimated changes in annual global mean near-surface air temperature. Stippling in (C) is the same as in Fig. 2(C) rather than based on the results of statistical test with respect to relative bias.

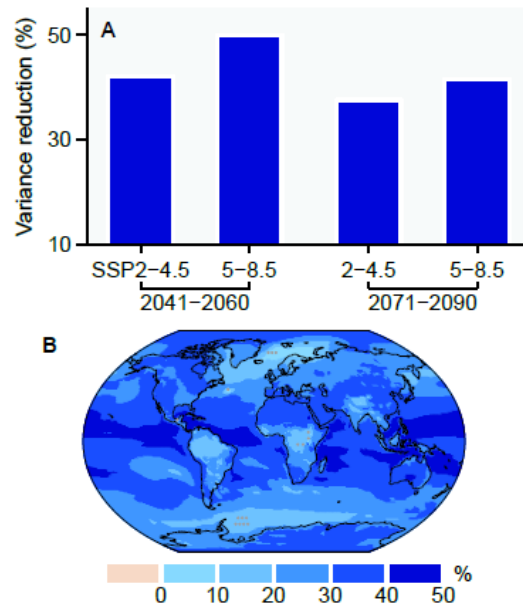


Fig. S4. Model-based evaluation of the constrained level-of-global warming approach in reducing projection uncertainty. (A) Percentage reductions in the variance of the estimated changes in annual global mean near-surface air temperature during 2041–2060 and 2071–2090 under SSP2–4.5 and SSP5–8.5 scenarios in “cool models” using “hot models” and the constrained level-of-global warming approach. (B) The counterpart of (A) but for model grid cell values, averaged across projection periods and emissions scenarios. Stippling in (B) indicates locations where the constrained level-of-global warming approach does not significantly reduce projection variance in one or more of the four considered scenario periods according to a sign test at the 5% level, which suggests significant projection variance reduction by the constrained level-of-global warming approach if it produces smaller projection variance for estimated warming for 8 or more of the 10 “cool models”.

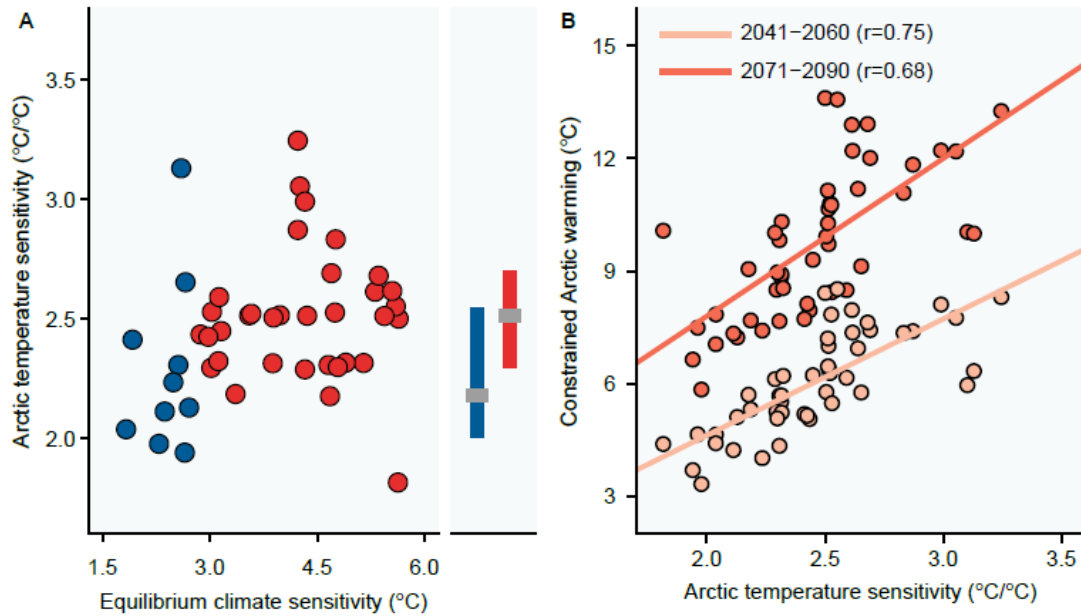


Fig. S5. A comparison of “hot” and “cool” models in the Arctic region. (A) Scatter plot shows the equilibrium climate sensitivity and Arctic temperature sensitivity to global warming in “hot” (red) and “cool” (blue) models, with one point for each model. Estimates of the equilibrium climate sensitivity in ref. 4 are adopted. The vertical and horizontal bars in the right panel mark the 16-84% uncertainty ranges and medians of the Arctic temperature sensitivity values in the “hot” (red) and “cool” (blue) models. The Arctic temperature sensitivity is defined by the ratio of the trend in the average annual mean near-surface air temperatures in the Arctic region (i.e., north of 65°N) to the trend of global warming over the period 1850-2100, based on merged historical simulations and raw, unconstrained SSP5-8.5 projections. **(B)** Scatter plot showing the inter-model relationships between Arctic temperature sensitivity and Arctic warming during 2041-2060 (pink) and 2071-2090 (orange) relative to 1850-1900, based on merged historical simulations and constrained SSP5-8.5 projections via the constrained-level-of-global warming approach. The strong inter-model relationships suggest that applying observational constraints for Arctic temperature sensitivity to the constrained Arctic warming projections may further reduce Arctic warming projection uncertainty.

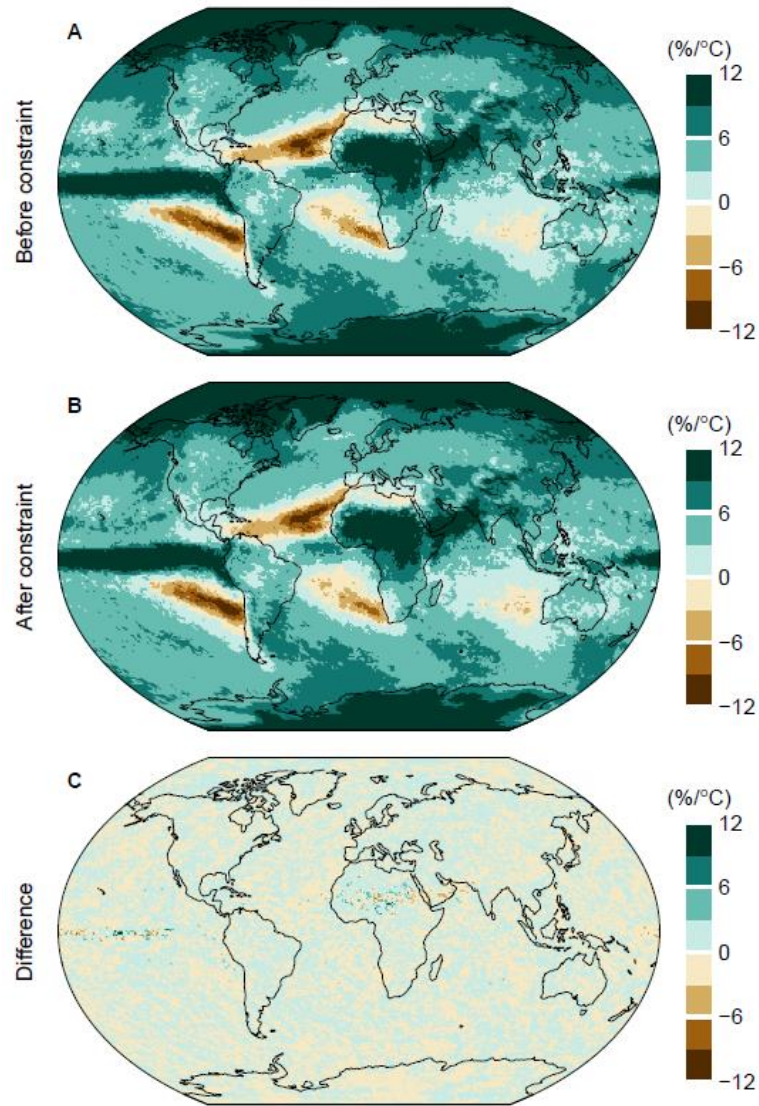


Fig. S6. Comparison of the scaling of extreme precipitation changes with global warming before and after constraint. Panels show the projected multi-model ensemble median scaling of changes in annual maximum daily precipitation with global warming before (A) and after (B) applying the constrained level-of-global warming approach, as well as their difference (C). For each model, the scaling is estimated by normalizing the unconstrained or constrained extreme precipitation changes during 2071-2090 relative to 1850-1900 by the corresponding unconstrained or constrained global warming respectively under the SSP5-8.5 emissions scenario.

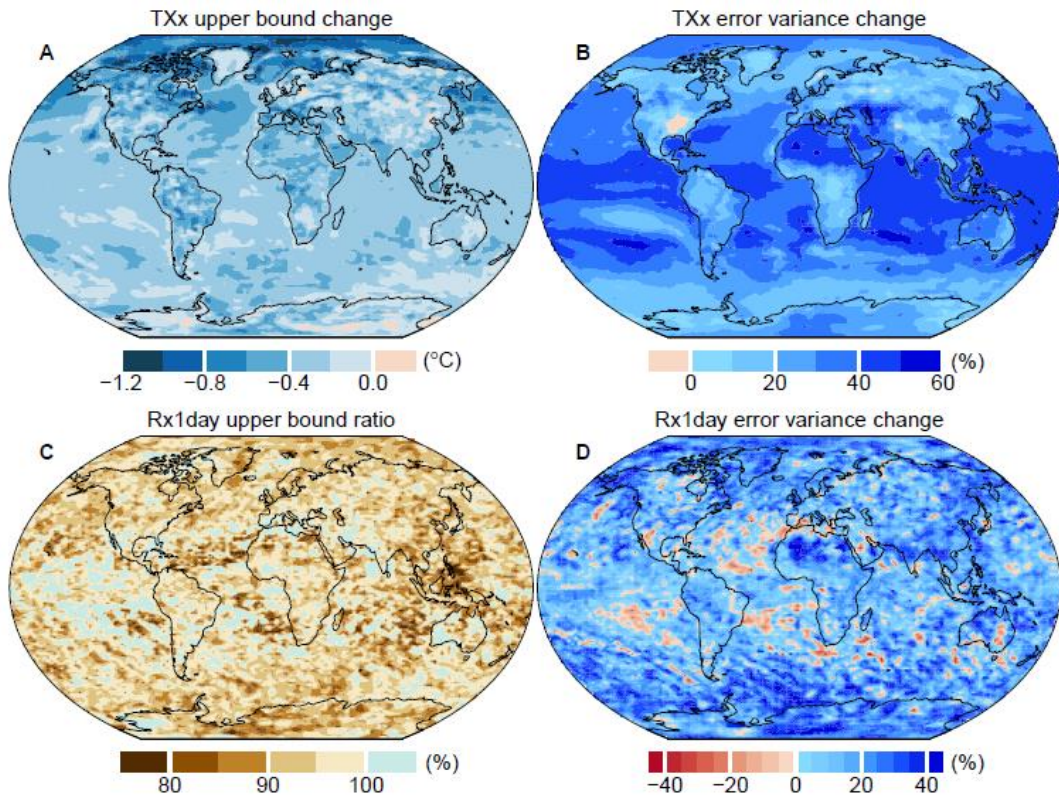


Fig. S7. Changes in the uncertainty of constrained temperature and precipitation extremes. (A-B) Differences in the upper bounds of the 16-84% uncertainty range of the projected changes in annual maximum daily temperature (TXx; **A**) and precipitation (Rx1day; **B**) during 2071-2090 under the SSP5-8.5 scenario relative to 1850-1900 by the constrained level-of-global warming approach with compared to unconstrained projections. For Rx1day, the differences are expressed as percentage ratios of the constrained upper bounds relative to the unconstrained upper bounds. (C-D) Percentage differences in the variances of the corresponding projected changes in TXx (**C**) and Rx1day (**D**).

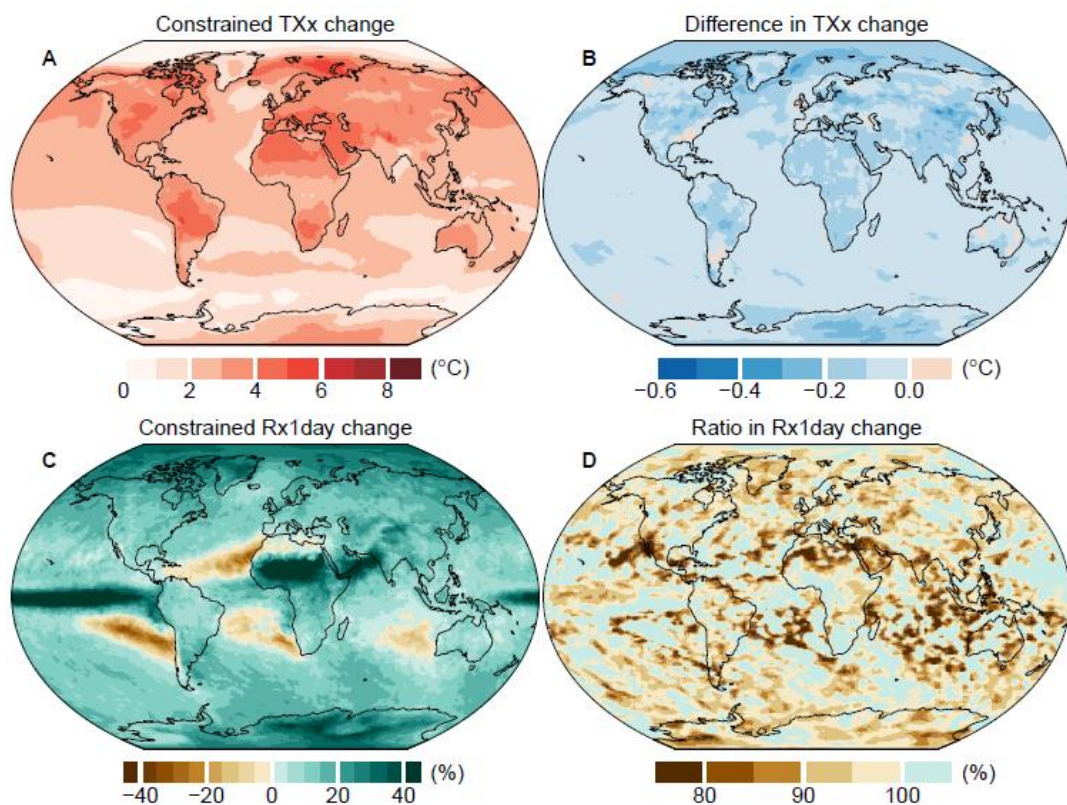


Fig. S8. Constrained future changes in temperature and precipitation extremes under SSP2-4.5. As in Fig. 3 in the main text, but for the projected changes under the SSP2-4.5 emissions scenario.

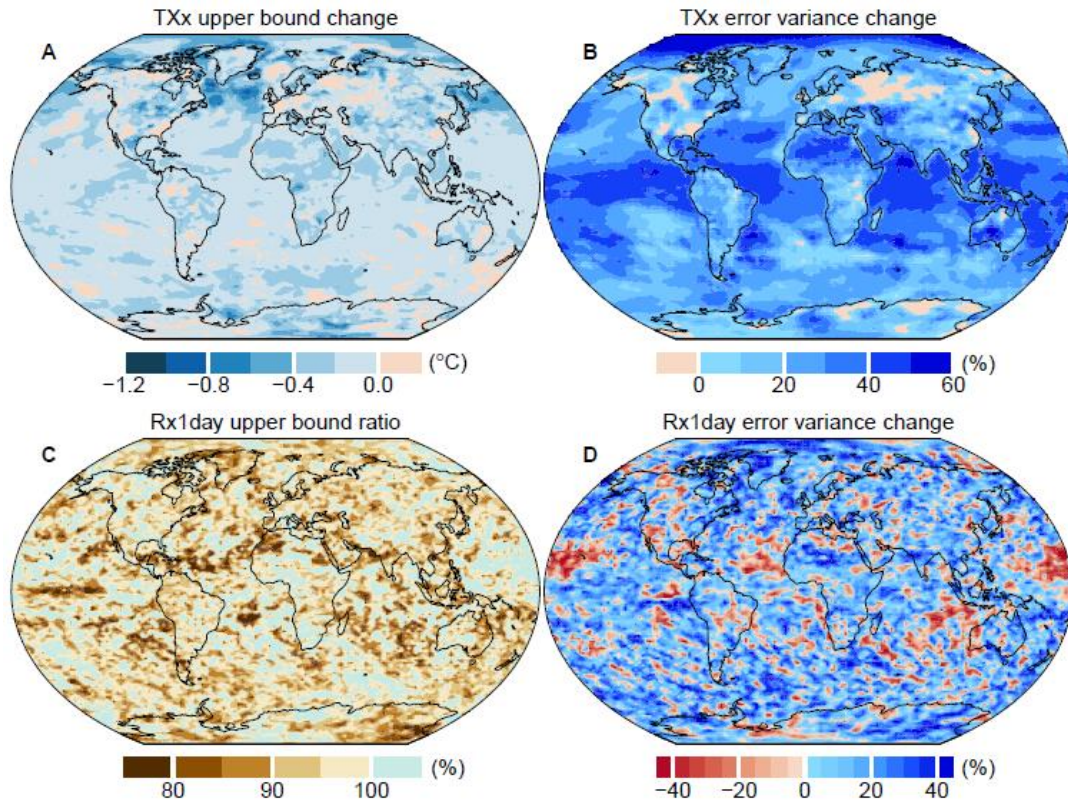


Fig. S9. Changes in the uncertainty of constrained temperature and precipitation extremes under SSP2-4.5. As in Fig. S7, but for the projected changes under the SSP2-4.5 emissions scenario.

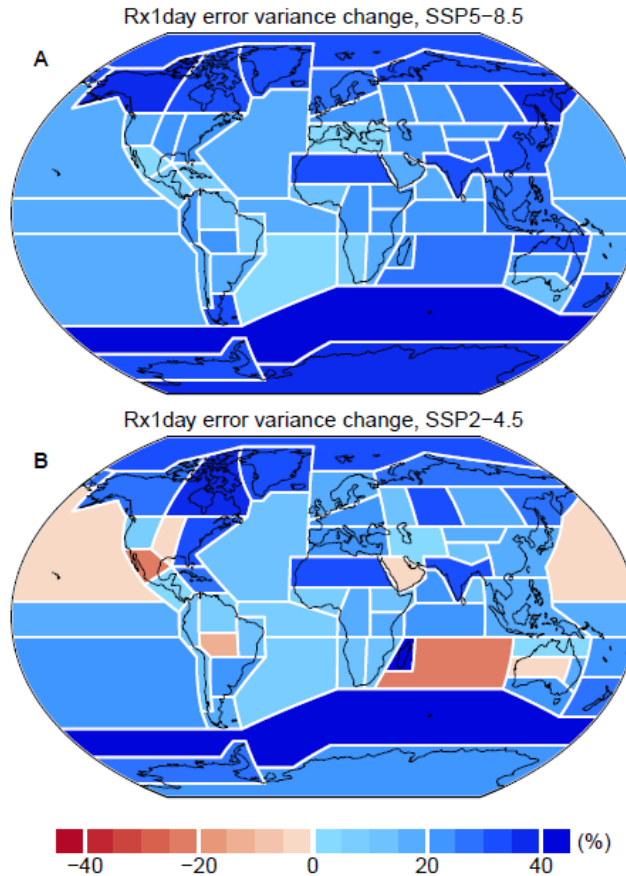


Fig. S10. Changes in the uncertainty of constrained regional precipitation extremes. Panels show the percentage differences in the variances of the projected regional changes in annual maximum daily precipitation (Rx1day) for IPCC AR6 regions during 2071-2090 under the SSP5-8.5 (A) and SSP2-4.5 (B) emissions scenarios relative to 1850-1900 by the constrained level-of-global warming approach compared to unconstrained projections. Regional extreme precipitation changes are defined as the mean of changes at individual grid cells within a region. Geographic boundaries of these regions are defined in ref. 46.

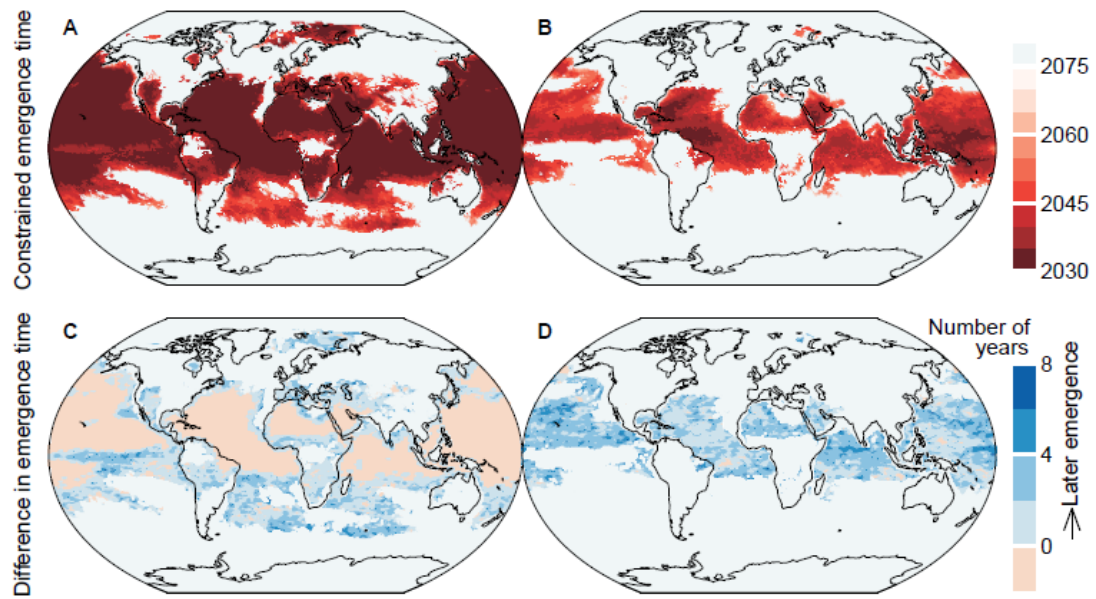


Fig. S11. Constrained time when the present-day extreme temperature event becomes a normal event. As in Fig. 4 in the main text, but for results under the SSP2-4.5 emissions scenario.

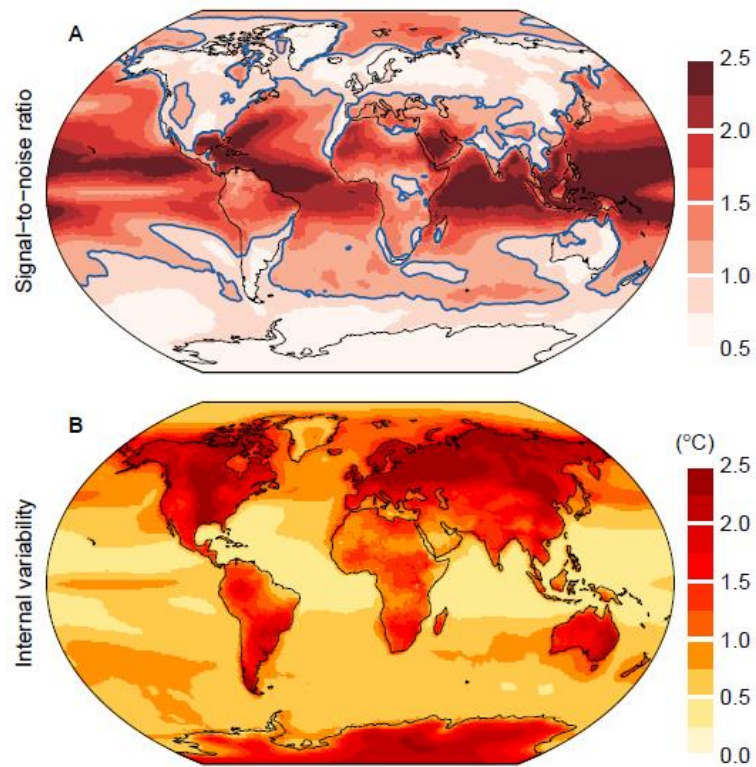


Fig. S12. The signal-to-noise ratio of changes in temperature extremes relative to internal variability. (A) The multi-model ensemble median ratio of the projected long-term trend in annual maximum daily temperature (TXx) during 2021-2090 as a function of global warming with respect to the standard deviation of TXx residuals after removing the long-term trend. The blue contour line marks a ratio of one. **(B)** The multi-model ensemble median standard deviation of TXx residuals.

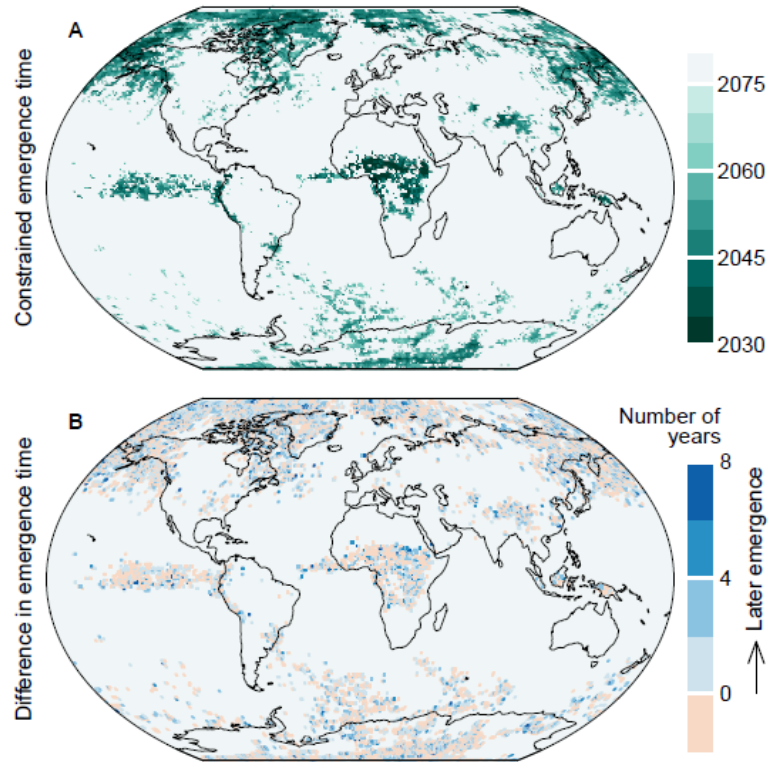


Fig. S13. Constrained time when present-day precipitation extreme event would double in frequency. Projected multi-model ensemble median time when the 50-year extreme annual maximum precipitation event in the present-day (1951-2020) climate would become 2 or more times as likely under the SSP5-8.5 emissions scenario estimated by the constrained level-of-global warming approach (A), and the differences compared to the time estimates from unconstrained projections (B).

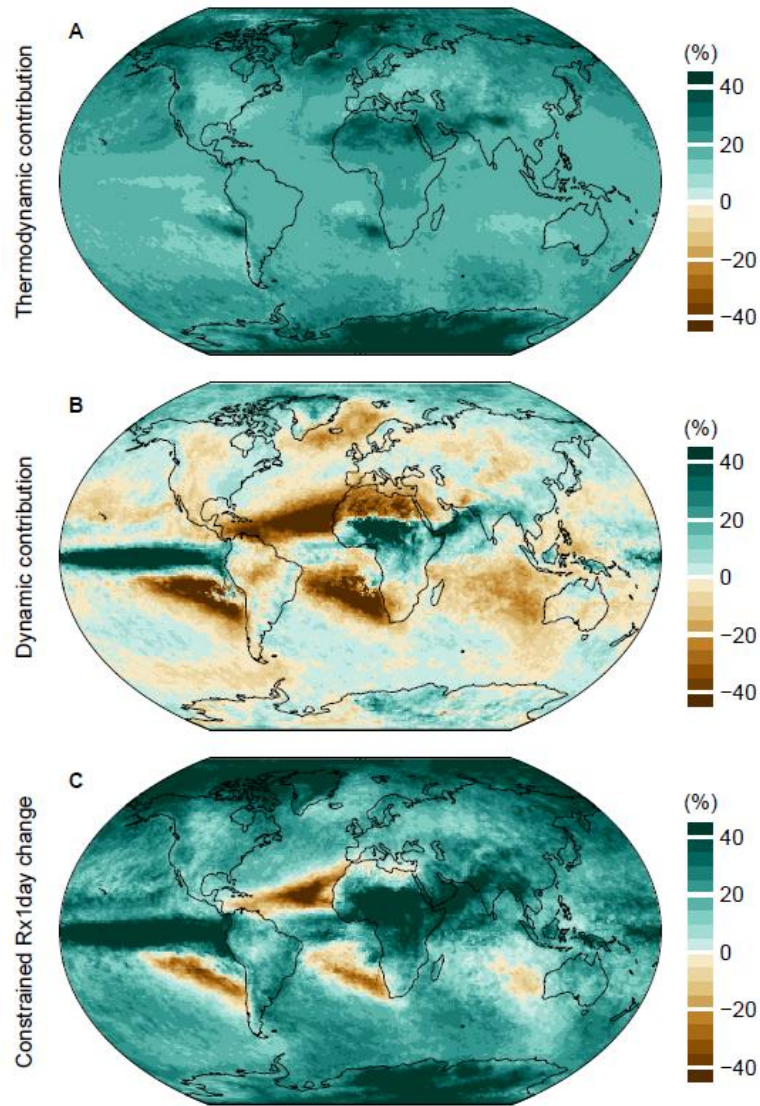


Fig. S14. Thermodynamic and dynamic contributions to the constrained extreme precipitation changes. The multi-model ensemble median thermodynamic (A) and dynamic contributions (B) to the projected changes in annual maximum daily precipitation (Rx1day) during 2071-2090 under the SSP5-8.5 emissions scenario relative to the 1850-1900 diagnosed from constrained projections by the constrained level-of-global warming approach. Compared to Fig 3(C), the results here are based on a smaller set of 14 Earth System models that include necessary simulations for diagnosing thermodynamic and dynamic contributions to extreme precipitation changes. The considered models are: CAMS-CSM1-0 (1 member), CanESM5 (20), CESM2 (1), CESM-WACCM (3), CMCC-CM2-SR5 (1), CMCC-ESM2 (1), FGOALS-g3 (2), MIROC6 (3), MIROC-ES2H (3), MIROC-ES2L (1), MPI-ESM1-2-HR (2), MPI-ESM1-2-LR (30), NorESM2-LM (1), NorESM2-MM (1). For reference,

the constrained multi-model ensemble median changes in annual maximum daily precipitation for these models are shown in (C).

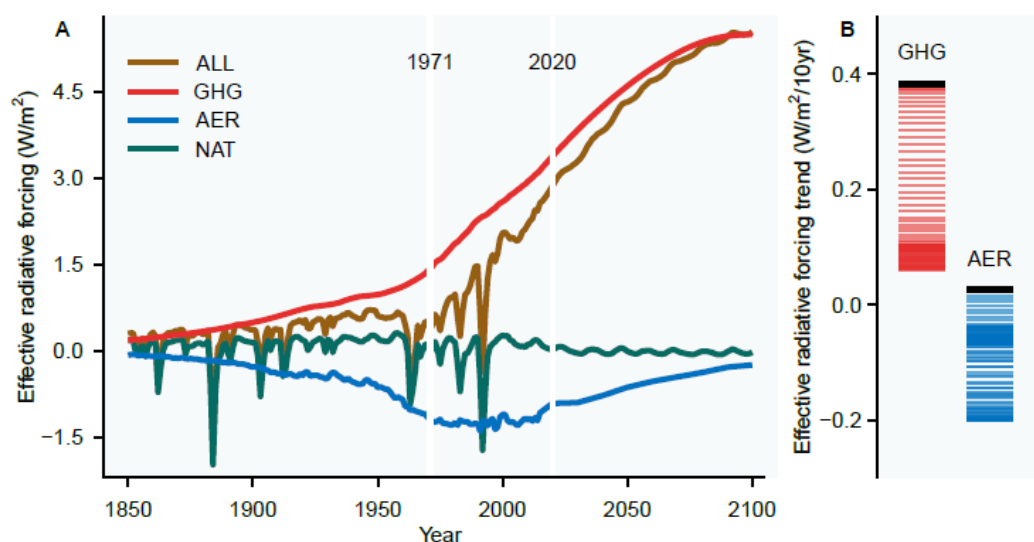


Fig. S15. Effective radiative forcing of different forcing agents. (A) Times series of the estimated effective radiative forcing from all-known (natural and anthropogenic; brown line), anthropogenic greenhouse gases (red), anthropogenic aerosols (blue), and natural (green) forcing agents according to ref. 63. (B) Trends of the effective radiative forcing of anthropogenic greenhouse gases (red) and aerosols (blue) during all possible 50-year segments in 1850-2100, with one horizontal line representing each segment. The black lines mark the corresponding values for the period 1971-2020.

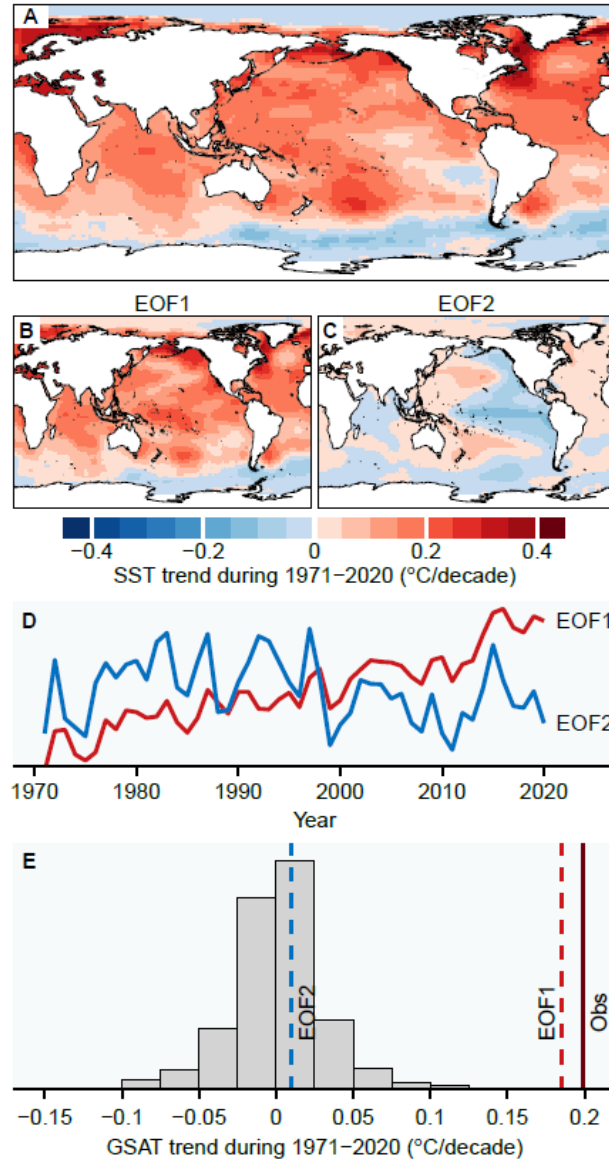


Fig. S16. An evaluation of the pattern effect of sea surface temperature changes on the observed warming. (A) The observed annual mean sea surface temperature trends during 1971-2020, based on the Extended Reconstructed Sea Surface Temperature v5 data. (B-C) The first two empirical orthogonal functions (EOFs) of the observed annual mean sea surface temperature fields, which explain about 31% and 21% of total variance, respectively. (D) The principal components corresponding to the first two EOFs. (E) Trend in GMST from HadCRUT5 observations for 1971-2020 (dark red solid line) and variations associated with the first two EOFs (red and blue dashed lines), as well as a histogram of 50-year GMST trends estimated from pre-industrial simulations.

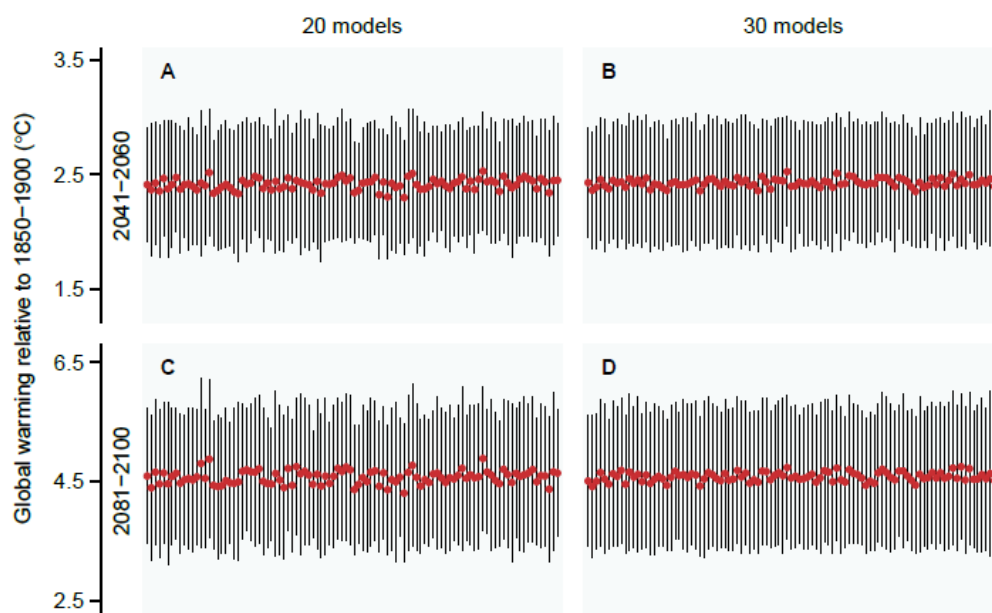


Fig. S17. Sensitivity of the constrained warming projections to the composition of the Earth system model ensemble. Panels show the means (red points) and 5-95% ranges (black lines) of the constrained warming projections for the SSP5-8.5 scenario periods of 2041-2060 and 2081-2100 relative to 1850-1900 using randomly selected Earth system model ensembles consisting of 20 and 30 models.

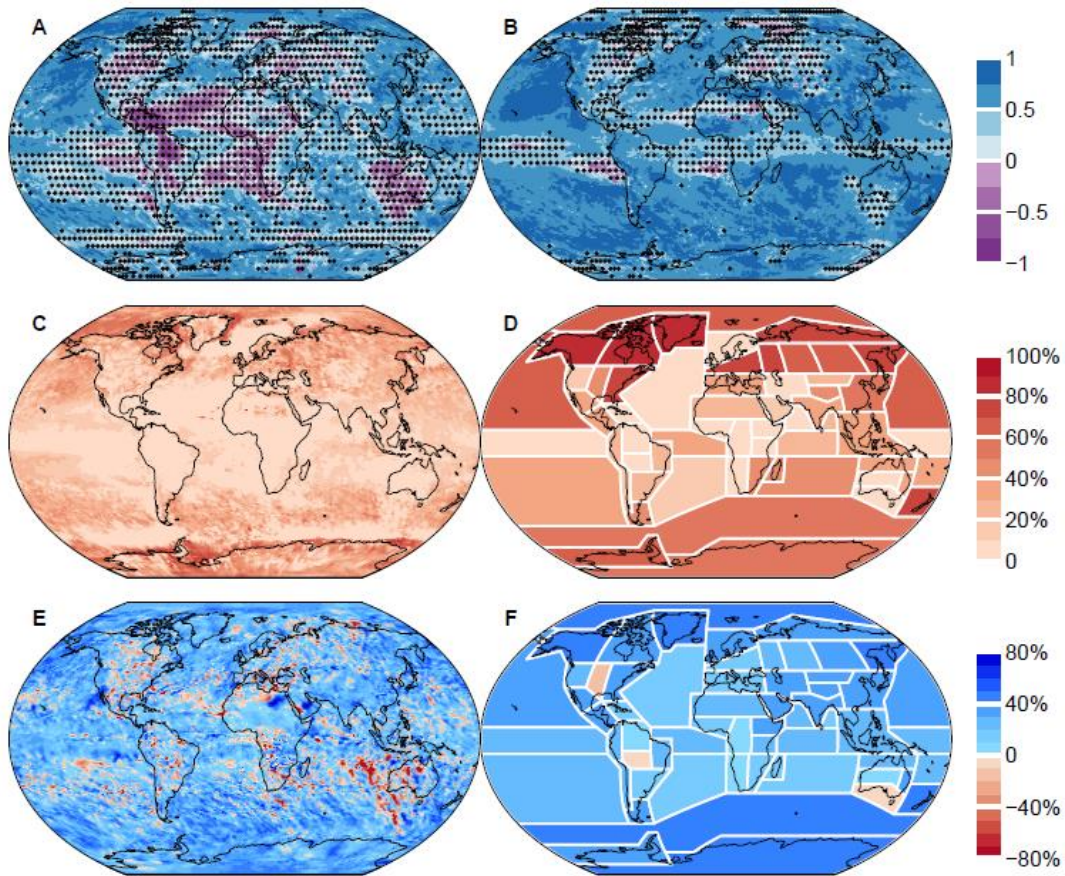


Fig. S18. Physical basis for the constrained level-of-global warming approach for extreme precipitation. (A-B) Inter-model correlations between trends in global mean surface air temperatures during 1971-2020 and the diagnosed total (A) and thermodynamic (B) changes in annual maximum daily precipitation during 2071-2090 relative to 1850-1900 under the SSP5-8.5 scenario. Statistically insignificant correlations at the 5% level are marked with stippling. (C-D) Percentage contributions of the projection error variance associated with the thermodynamic components of extreme precipitation changes at local (C) and regional (D) scales to the total projection error variance, calculated as 100% minus the proportion of projection error variance of the dynamic changes, based on raw, unconstrained projections. Regional extreme precipitation changes are defined as the mean of changes across individual grid cells within a region. Geographic boundaries of these regions are defined in ref. 46. (E-F) Percentage differences in the variances of the projected extreme precipitation changes at local (E) and regional (F) scales by the constrained level-of-global warming approach compared to unconstrained projections. Despite increases in

projection error variance in some grid cells due to internal climate variability, the constrained level-of-global warming approach reduces approximately half of the projection error variance associated with the thermodynamic components of extreme precipitation changes. The results are based on Earth System models with necessary simulations for diagnosing thermodynamic and dynamic contributions to extreme precipitation changes. The 14 models considered include: CAMS-CSM1-0 (1 member), CanESM5 (20), CESM2 (1), CESM-WACCM (3), CMCC-CM2-SR5 (1), CMCC-ESM2 (1), FGOALS-g3 (2), MIROC6 (3), MIROC-ES2H (3), MIROC-ES2L (1), MPI-ESM1-2-HR (2), MPI-ESM1-2-LR (30), NorESM2-LM (1), NorESM2-MM (1). Differences between the results in (E-F) and those in Figs. S7(D) and S10(A) are due to the inclusion of more Earth system models in the latter figures, which are based on the 20 models listed in Table S2.

Table S1. List of models used for the derivation of constrained warming. The estimates of equilibrium climate sensitivity (ECS) are adopted from ref. 4. All listed models provide necessary simulations for the computation of annual mean near-surface air temperature under the SSP5-8.5 scenario, while those that also provide the necessary SSP2-4.5 simulations are marked in bold. The numbers in the parentheses indicate ensemble size of the available SSP2-4.5 simulations from the corresponding models. Asterisks denote “cool” models considered in this study according to their ECS values.

| Models | ECS (°C) | Number of runs | Models | ECS (°C) | Number of runs |
|-------------------------|-------------|-------------------|----------------------|-------------|-------------------|
| ACCESS-CM2 | 4.66 | 5 (5) | ACCESS-ESM1-5 | 3.88 | 35 (10) |
| AWI-CM-1-1-MR | 3.16 | 1 (1) | BCC-CSM2-MR | 3.02 | 1 (1) |
| CAMS-CSM1-0* | 2.29 | 2 (2) | CanESM5 | 5.64 | 50 (50) |
| CanESM5-CanOE | 5.60 | 3 (3) | CAS-ESM2-0 | -- | 2 (2) |
| CESM2 | 5.15 | 3 (3) | CESM2-WACCM | 4.68 | 3 (3) |
| CIESM | 5.63 | 1 (1) | CMCC-CM2-SR5 | 3.55 | 1 (1) |
| CMCC-ESM2 | 3.58 | 1 (1) | CNRM-CM6-1 | 4.90 | 6 (6) |
| CNRM-CM6-1-HR | 4.33 | 1 (1) | CNRM-ESM2-1 | 4.79 | 5 (9) |
| E3SM-1-1 | 5.31 | 1 | EC-Earth3 | 4.26 | 8 (22) |
| EC-Earth3-CC | 4.23 | 1 (1) | EC-Earth3-Veg | 4.33 | 7 (8) |
| EC-Earth3-Veg-LR | 4.23 | 3 (3) | FGOALS-f3-L | 3.98 | 1 (1) |
| FGOALS-g3 | 2.87 | 4 (4) | FIO-ESM-2-0 | - | 3 (3) |
| GFDL-CM4 | 3.89 | 1 (1) | GFDL-ESM4* | 2.65 | 1 (3) |
| GISS-E2-1-G* | 2.71 | 10 (14) | GISS-E2-1-H | 3.12 | 4 (10) |
| HadGEM3-GC31-LL | 5.55 | 4 (1) | HadGEM3-GC31-MM | 5.44 | 4 |
| IITM-ESM* | 2.37 | 1 (1) | INM-CM4-8* | 1.83 | 1 (1) |
| INM-CM5-0* | 1.92 | 1 (1) | IPSL-CM6A-LR | 4.70 | 6 (11) |
| KACE-1-0-G | 4.75 | 3 (3) | KIOST-ESM | 3.36 | 1 (1) |
| MCM-UA-1-0 | - | 1 (1) | MIROC6* | 2.60 | 50 (33) |
| MIROC-ES2H | - | 3 (3) | MIROC-ES2L* | 2.66 | 10 (30) |
| MPI-ESM1-2-HR | 2.98 | 2 (2) | MPI-ESM1-2-LR | 3.03 | 10 (10) |
| MRI-ESM2-0 | 3.13 | 6 (5) | NESM3 | 4.76 | 2 (2) |
| NorESM2-LM* | 2.56 | 1 (3) | NorESM2-MM* | 2.49 | 1 (2) |
| TaiESM1 | 4.36 | 1 (1) | UKESM1-0-LL | 5.36 | 5 (14) |

Table S2. List of models used for the storyline analysis of changes in temperature and precipitation extremes. The numbers indicate ensemble size of the analyzed SSP5-8.5 simulations. Although the HadGEM3-GC31-LL, HadGEM3-GC31-MM, KACE-1-0-G, and UKESM1-0-LL models have necessary output for computing the analyzed temperature and precipitation extremes, they were excluded from the analysis to avoid the influence of erroneously generated daily maximum temperature outliers in these models (e.g., see <https://errata.ipsl.fr/static/view.html?uid=76b3f818-d65f-c76b-bfd8-cae5bc27825c> for a description of outliers in MetOffice Hadley Centre models; a similar, but undocumented problem affects KACE-1-0-G simulations).

| Model | Number of runs | Model | Number of runs |
|---------------|----------------|---------------|----------------|
| ACCESS-CM2 | 1 | ACCESS-ESM1-5 | 1 |
| BCC-CSM2-MR | 1 | CanESM5 | 50 |
| CNRM-CM6-1 | 1 | CNRM-CM6-1-HR | 1 |
| CNRM-ESM2-1 | 1 | EC-Earth3 | 7 |
| EC-Earth3-Veg | 1 | GFDL-ESM4 | 1 |
| INM-CM4-8 | 1 | INM-CM5-0 | 1 |
| KIOST-ESM | 1 | MIROC-ES2L | 1 |
| MIROC6 | 50 | MPI-ESM1-2-HR | 1 |
| MPI-ESM1-2-LR | 10 | MRI-ESM2-0 | 1 |
| NESM3 | 1 | NorESM2-MM | 1 |

Table S3. List of models used for fingerprinting analysis on the observed warming. The numbers indicate ensemble size of the simulations forced by historical all forcings, greenhouse gases changes, and aerosol changes, respectively. Only models having at least 3 simulations for the period 1901-2020 and all considered forcing agents are analyzed. For models which do not have historical all-forcing simulations after 2014, the SSP5-8.5 simulations by the corresponding models are used for extension.

| Model | Number of runs |
|-----------------|----------------|
| ACCESS-CM2 | 5, 3, 3 |
| ACCESS-ESM1-5 | 10, 3, 3 |
| CanESM5 | 50, 50, 30 |
| CNRM-CM6-1 | 6, 9, 10 |
| FGOALS-g3 | 4, 3, 3 |
| HadGEM3-GC31-LL | 4, 4, 3 |
| IPSL-CM6A-LR | 6, 10, 10 |